Supporting Information

A Thermochromic Polyoxovanadate with a 200,000-fold Conductivity Gain for Boosting Zinc-Ion Batteries Performance

Ze-Xun Zhang,[a+] Xiao-Yue Zhang,[a+] Ping-Wei Cai,*[a] Cai Sun,*[a,b] and Shou-Tian Zheng*[a]

a Fujian Provincial Key Laboratory of Advanced Inorganic Oxygenated-Materials
College of Chemistry
Fuzhou University
Fuzhou, Fujian 350108, China
E-mail: cai2022@fzu.edu.cn; csun@fzu.edu.cn; stzheng@fzu.edu.cn
b Fujian Science & Technology Innovation Laboratory for Optoelectronic Information of China
Fuzhou, Fujian 350108, China
+ These authors contributed equally to this work.

Experimental Procedures

Materials and Methods

Materials

$MVCl_2$ was synthesized as described in the literature.[1] Other chemicals were used as purchased without further purification.

Measurements

Infrared (IR) spectra (KBr pellet) were performed on an Opus Vetex 70 FTIR infrared spectrophotometer in the range of 400-4000 cm^{-1}. Powder X-ray diffraction (PXRD) patterns were recorded on a Rigaku MiniFlex 600 diffractometer with Cu *K*α radiation (*λ* = 1.54056 Å). Simulated PXRD data was simulated by the Mercury Software with the step of 0.02° from 5° to 50° (*λ* = 1.54056 Å). Thermogravimetric analyses were conducted using a Mettler Toledo TGA/DSC 3+ analyzer in an N_2-flow atmosphere with a heating rate of 10 °C/min at a temperature of 30–800 °C. ICP-OES analysis was conducted on an Ultima2 spectrometer, and the crystal samples were vacuum dried at 80 °C for 2 h before ICP testing. The UV-Vis spectra were measured on a SHIMADZU UV-2600 and SHIMADZU UV-3600i plus by using the $BaSO_4$ as the blank. Single-crystal X-ray diffraction measurements were performed on Rigaku XtaLAB Synergy-R, using graphite monochromated Mo *Kα* radiation (*λ* = 0.71073 Å).

X-ray crystallography

Single-crystal X-ray diffraction measurements were performed on Rigaku XtaLAB Synergy-R, using graphite monochromated Mo K_α radiation (*λ* = 0.71073 Å). Intensity data sets were collected using *ω* scan techniques and corrected for *Lp* effects. The structures were solved by the direct method and refined by full-matrix least squares on F^2 using the Siemens SHELXTL™ Version 5 package of crystallographic software with anisotropic thermal parameters for all non-hydrogen atoms. Hydrogen atoms were added geometrically and refined using the riding model. Crystal data and structure refinement results for MV_2V_{10} are summarized in Table S1.

Synthesis of $MV_2[H_2V_{10}O_{28}]$ (MV_2V_{10})

A mixture of NH_4VO_3(0.080 g, 0.69 mmol) and methyl viologen dichloride (0.180 g, 0.42 mmol) was mixed in 8 mL deionized water. After stirring for 1 hours, the mixture was sealed in a 25 mL Teflon-lined autoclave and heated at 120 °C for 3 d. After cooling to room temperature, allowed to stand undisturbed for a period of time, the filtrate slowly evaporates at room temperature for one week, yielding yellow rod-like crystals. Subsequent annealing of these crystals at 120 °C for 3 hours yielded compound MV_2V_{10}. Yield: ~ 20 mg (20.3%, based on NH_4VO_3). Elemental analysis calcd (found %) for MV_2V_{10}-a: C, 21.67 (21.72); H, 2.11 (2.23); N, 4.22 (4.31), V, 38.3 (38.8) and MV_2V_{10}-b: C, 21.67 (21.98); H, 2.11 (2.22); N, 4.22 (4.33), V, 38.3 (38.9).

Synthesis of $EQ_4[H_2V_{10}O_{28}]\cdot H_2O$ (EQ_4V_{10})

A mixture of $NaVO_3$(0.090 g, 0.73 mmol) and ethyl viologen dichloride (0.050 g, 0.23 mmol) was mixed in 8 mL deionized water. After stirring for 1 hour, the mixture was sealed in a 25 mL Teflon-lined autoclave and heated at 140 °C for 3 d. After cooling to room temperature, allowed to stand undisturbed for a period of time, the filtrate slowly evaporates at room temperature for ten days. yielding yellow sheet-like crystals. Yield: ~ 10 mg (24.4%, based on $NaVO_3$).

Electrical Testing

Temperature-dependent electrical conductivities and *I*–*V* curves were measured in a Keithley 2636B semiconductor parameter analyzer using single crystal and pellet samples by the two probe method using silver paste, and in situ heating was also performed on this instrument. For the Hall-effect measurements, the powdered sample was compacted into circular pellets of 1 cm in diameter. The electrical transport properties of these pellets were then characterized by a Keithley ET9000. Hall effect measurement system under a specified magnetic field (1.2 T) and temperature (298 K).

Material Preparation and Electrochemical Testing

The cathode MV_2V_{10}-b was prepared by mixing MV_2V_{10}-b, acetylene black, and PVDF in a weight ratio of 7:2:1. An appropriate amount of NMP (N-methyl-2-pyrrolidone) was added to form a slurry. The slurry was uniformly coated onto a titanium foil and then dried under vacuum for 12 hours to obtain the final cathode composite. The anode was 100 μm zinc foil. The separator used was Whatman GF/D, and the electrolyte was 3M $Zn(OTF)_2$. All the batteries were assembled in CR2032-type coins at room temperature. The electrochemical impedance spectroscopy (EIS) was tested at a constant frequency range between 10^{-2} – 10^5 Hz. The coin-type batteries were tested for cyclic voltammetry using a CHI660E electrochemical workstation. The three-electrode system was employed to measure cyclic voltammetry using a Zennium-pro (Germany Zahner Instrument), the CV plot used to estimate the energy bonds positions was tested in 0.2 M $KHCO_3$ electrolyte at the scan rate of 20 mV s^{-1}.

The analyses of capacitive control: the square root of the peak current (*i*) is not well proportional to the scan rate (*v*), indicating a combination of non-Faraday and Faraday behaviors in the charge/discharge process. On the basis of a previous study,[2] the correlation equation between *i* and *v* is as follows:

$$i = av^b \#(1)$$

$$\log(i) = blog(v) + \log(a) \#(2)$$

where *a* and *b* are adjustable parameters. When the value of *b* is 0.5, ion diffusion dominates the charge/discharge process.

The proportion of the Zn^{2+} capacitance effect can be further quantified by dividing the current response *i* at a fixed potential into a capacitance effect and a diffusion control response $k_2v^{0.5}$. The capacitive effect can be calculated via the following equation: [3]

$$i = k_1 v + k_2 v^{1/2} \#(3)$$

GITT test: For GITT analyses, the cells were cycled in the potential window of 0.2-1.9 V *vs.* Zn/Zn^{2+} at 20 mA g^{-1}. The duration time for each applied galvanostatic current was 10 min and then the cell was relaxed for 20 min. The apparent chemical diffusion coefficients values can be calculated according to the following equation: [4]

$$D_{GITT} = \frac{4}{\pi\tau}\left(\frac{m_B V_M}{M_B S}\right)^2\left(\frac{\Delta E_s}{\Delta E_\tau}\right)^2 \#(4)$$

where m_B V_M and M_B are the mass, molar volume and molecular weight of the MV_2V_{10}-b, respectively. τ is the time for an applied galvanostatic current; S is the contacting area of the electrode; ΔE_s and ΔE_τ are the quasi-equilibrium potential and the change of cell voltage during the galvanostatic current pulse, respectively.

Computational approaches

The BS and PDOS calculations were based on the density functional theory in conjunction with the projector-augmented-wave potential, which is implemented in the Vienna ab initio Simulation Package.[5] The Perdew−Burke−Ernzerh of exchange-correlation functionals was used.[6] The crystallographic data of MV_2V_{10} was applied to build calculation models with a plane-wave cutoff energy of 400 eV and a 3 × 2 × 3 Monkhorst–Pack grid of k-points. All atoms were allowed to relax until the forces fell below 0.01 eV $Å^{-1}$.

The molecular model of V_{10} was taken from the above optimized structure of MV_2V_{10} for below DFT calculations (Fig S10). The DFT calculations of the wave function for MV_2V_{10}-a and MV_2V_{10}-b were done in Gaussian 09 D01 version[7] using the PBE functional with 6-311G* and SDD basis sets for O and Mo, respectively. The analysis of wave function for electron density difference, ADCH charge, and Hirshfeld charge were derived using the Multiwfn software.[8] Electron density difference calculations were conducted on the basis of the following equation: $\Delta\rho = \rho_{V10\text{-}b} - \rho_{V10\text{-}a}$, where $\rho_{V10\text{-}a}$ and $\rho_{V10\text{-}b}$ were electron densities of the MV_2V_{10}-a and MV_2V_{10}-b, respectively.

Supplementary Tables.

Table S1. Crystal and structure refinement data for MV_2V_{10}-a and MV_2V_{10}-b.

	MV_2V_{10}-a	MV_2V_{10}-b
Formula	$C_{24}H_{30}N_4O_{28}V_{10}$	$C_{24}H_{30}N_4O_{28}V_{10}$
Mr	1329.90	1329.90
Crystal size (mm^3)	0.13× 0.11 × 0.10	0.13× 0.11 × 0.10
Crystal system	monoclinic	monoclinic
Space group	$P2_1/n$	$P2_1/n$
***a* (Å)**	10.0360(2)	10.0240(2)
***b* (Å)**	15.9655(3)	15.9986(3)
***c* (Å)**	11.9170(2)	11.9042(2)
α (deg)	90	90
β (deg)	91.246(2)	91.101(2)
γ (deg)	90	90
***V* (Å^3)**	1909.01(6)	1908.72(6)
D_{calcd} (g/cm^3)	2.314	2.314
Z	2	2
***F*(000)**	1038.0	1308.0
Abs coeff (mm^{-1})	2.439	2.440
Refund collcd/unique (R_{int})	43032/5101 (0.0426)	37357/4681 (0.0583)
Data/params/restraints	5101/0/300	4681/0/300
R_1[a]	0.0388	0.0580
ωR_2[b]	0.0835	0.1322
GOF on F^2	1.136	1.180
$\Delta\rho_{max}$ and $\Delta\rho_{min}$ (e/Å^3)	1.02 and -0.56	1.75 and -0.79

[a]$R_1 = \sum||F_o|-|F_c||/\sum|F_o|$, [b]$\omega R_2 = \{\sum\omega[(F_o)^2-(F_c)^2]^2/\sum\omega[(F_o)_2]^2\}^{1/2}$.

Table S2. Comparative analysis of bond lengths between MV_2V_{10}-a and MV_2V_{10}-b.

bond	bond length of MV_2V_{10}-a (Å)	bond length of MV_2V_{10}-b (Å)
C10-C11	1.370(5)	1.370(9)
C2-C1	1.380(5)	1.376(9)
C3-C2	1.400(5)	1.401(9)
C4-C3	1.385(5)	1.377(9)
C4-C5	1.384(5)	1.385(9)
C7-C8	1.379(5)	1.382(9)
C9-C8	1.398(5)	1.394(9)
C9-C10	1.400(5)	1.392(9)
C9-C3	1.483(5)	1.486(9)
N1-C5	1.350(4)	1.362(8)
N1-C1	1.342(4)	1.349(8)
N1-C6	1.484(4)	1.478(8)
N2-C7	1.346(5)	1.340(8)
N2-C12	1.489(4)	1.488(8)
N2-C11	1.350(5)	1.353(8)
V1-O13[1]	2.305(2)	2.300(4)
V1-O4	2.053(2)	1.767(4)
V1-O14[1]	1.993(2)	1.996(4)
V1-O3	1.768(2)	2.051(4)
V1-O2	1.859(2)	1.855(4)
V1-O1	1.606(2)	1.604(4)
V2-O13[1]	2.325(2)	2.312(4)
V2-O6	1.949(2)	1.857(4)
V2-O11	2.063(2)	2.061(4)
V2-O2	1.782(2)	1.788(4)
V2-O8	1.858(2)	1.953(4)
V2-O7	1.609(2)	1.616(4)
V3-O13[1]	2.288(2)	2.240(4)
V3-O12	1.939(2)	1.899(4)
V3-O10[1]	2.024(2)	2.074(4)
V3-O3	1.901(2)	1.976(4)
V3-O8	1.786(2)	1.748(4)
V3-O9	1.605(2)	1.620(4)
V4-O13[1]	2.245(2)	2.288(4)
V4-O12[1]	2.071(2)	2.021(4)
V4-O4	1.977(2)	1.899(4)
V4-O10	1.901(2)	1.941(4)
V4-O6	1.742(2)	1.787(4)
V4-O5	1.620(2)	1.599(4)
V5-O13	2.102(2)	2.113(4)
V5-O13[1]	2.108(2)	2.108(4)
V5-O12	1.916(2)	1.956(4)
V5-O10	1.954(2)	1.913(4)
V5-O14	1.696(2)	1.692(4)
V5-O11	1.690(2)	1.689(4)

Table S3. Calculated ADC charge and Hirshfeld charge for initial (V_{10}-a) and charge separated state (V_{10}-b) of V_{10}.

Atom	ADC charge		Hirshfeld charge	
	V_{10}-a	V_{10}-b	V_{10}-a	V_{10}-b
1(V)	0.525271	0.502603	0.52068696	0.49556351
2(V)	0.52829	0.496832	0.5263207	0.4864589
3(V)	0.512829	0.505283	0.55525096	0.54490471
4(V)	0.518668	0.5053	0.52258985	0.50839318
5(V)	0.512942	0.506138	0.55537578	0.54597511
6(V)	0.525063	0.505713	0.52055683	0.49904793
7(V)	0.518542	0.507115	0.52248229	0.51015397
8(V)	0.52205	0.522449	0.51964021	0.51651016
9(V)	0.522065	0.522014	0.51952635	0.51589929
10(V)	0.528301	0.501269	0.5263226	0.49198376
11(O)	-0.375012	-0.355006	-0.35378485	-0.33386909
12(O)	-0.373533	-0.39718	-0.39579029	-0.41129839
13(O)	-0.345832	-0.278477	-0.33870258	-0.27406216
14(O)	-0.278921	-0.273873	-0.32098713	-0.31572211
15(O)	-0.268583	-0.264348	-0.31251057	-0.30838579
16(O)	-0.278646	-0.274394	-0.32086866	-0.31630581
17(O)	-0.268633	-0.263545	-0.31257999	-0.30807947
18(O)	-0.374727	-0.357845	-0.35370059	-0.33690067
19(O)	-0.344626	-0.305823	-0.34001002	-0.30316907
20(O)	-0.367952	-0.380965	-0.3920879	-0.40054791
21(O)	-0.345473	-0.288119	-0.33861693	-0.28355762
22(O)	-0.323368	-0.329283	-0.35435133	-0.35788112
23(O)	-0.362642	-0.36285	-0.35061229	-0.35064085
24(O)	-0.361364	-0.36628	-0.37940057	-0.38242746
25(O)	-0.36268	-0.363011	-0.35065963	-0.35079271
26(O)	-0.361603	-0.366828	-0.3795415	-0.38273456
27(O)	-0.344642	-0.300015	-0.34002215	-0.2976369
28(O)	-0.367725	-0.382762	-0.39197403	-0.40176153
29(O)	-0.32327	-0.329957	-0.35432467	-0.35834304
30(O)	-0.373982	-0.394497	-0.39603333	-0.40949179
31(O)	-0.390637	-0.389326	-0.33370921	-0.33486662
32(O)	-0.471355	-0.4755	-0.27690284	-0.27868635
33(O)	-0.390596	-0.389262	-0.33366074	-0.33447765
34(O)	-0.341641	-0.345878	-0.33140181	-0.33319683
35(O)	-0.341991	-0.348528	-0.32818533	-0.33159369
36(O)	-0.341596	-0.346471	-0.33141262	-0.33338146
37(O)	-0.342115	-0.347949	-0.3282635	-0.33138419
38(O)	-0.471524	-0.475112	-0.27694963	-0.27847016
39(H)	0.344197	0.342982	0.16807651	0.166211
40(H)	0.344303	0.343266	0.16806638	0.16644331

Table S4. Contrast reported to date for switchable bistable semiconductors.

Material	Method	Switch off (S cm^{-1})	Switch on (S cm^{-1})	Switch ratio	Ref.
MV_2V_{10}-b	thermoinduced	6.25×10^{-10}	1.28×10^{-4}	2.05×10^{5}	This Work
$(H_2bipy)(Hox)_2$	photoinduced	7.26×10^{-11}	1.86×10^{-9}	250	[9]
$\{[Pb_3Cl_6(CV)]\ H_2O]\}_n$	photoinduced	7.16×10^{-11}	1.23×10^{-7}	1720	[10]
diarylethene-based single-molecule junction	photoinduced	NA	NA	~100	[11]
$CsSnI_3$	thermoinduced	16	208	13	[12]
$[H_21]\ [H_2BPCH]\cdot H_2O]$	photoinduced	0.10 ±0.05	1.55 ±0.20	16	[6]
$((Me)_3pytpy)[BiCl_6]\cdot 2H_2O$	photoinduced	1.77×10^{-12}	9.34×10^{-12}	4	[13]
$((Me)_3pytpy)[Bi_2Cl_9]\cdot H_2O$	photoinduced	8.78×10^{-12}	2.47×10^{-11}	2	[13]
$\{(MV)_2[Pb_7Br_{18}]\}_n$	thermoinduced	1.30×10^{-9}	2.10×10^{-10}	5.8	[14]
$(AEV)[Pb_2Br_8]$	thermoinduced	5.58×10^{-8}	1.24×10^{-10}	450	[15]
$[(HDMA)_4(Pb_3Br_{10})(PhSQ)_2]_n$	photoinduced	8.92×10^{-9}	6.11×10^{-10}	14.6	[16]

Table S5. The reproducibility experiments of hall effect measurements by van der Pauw methods under the same condition (298 K, 1.2 T).

Sample No.	Hall coefficient (cm^3/C)	Hall carrier concentration (cm^{-3})	Hall electron mobility (cm^2/Vs)
1	-3.774887×10^{4}	1.653416×10^{14}	1.385370
2	-6.554461×10^{4}	9.522461×10^{13}	2.396977
3	-1.184127×10^{5}	5.270937×10^{13}	4.326157
4	-6.850045×10^{4}	9.111561×10^{13}	2.496723
Average	-7.255166×10^{4}	1.010978×10^{14}	2.651307

Table S6. The comparison of carrier concentration between this work and commercial semiconductors.

Materials	Carrier concentration (cm^{-3})
MV_2V_{10}-b	1.01×10^{14}
Si	1.5×10^{10}
Ge	2.4×10^{13}
GaAs	1.8×10^{6}

Table S7. The comparison of cycling stability between this work and other previous reports.

Materials	Current (A g^{-1})	Cycle number (n)	Capacity retention (%)	Ref.
MV_2V_{10}-b	2	1000	100	This work
MV_2V_{10}-b	10	5900	97.6	This work
$Na_2CaV_4O_{12}$ (NCVO)	10	5000	91.9	[17]
$Zn_{0.25}V_2O_5{\cdot}nH_2O$	2.4	1000	80	[18]
$ZnMn_2O_4$	0.5	500	94	[19]
HAVO-$FeMo_6$-50	0.5	100	85.4	[20]
V_2O_3-CC	10	5000	71.0	[21]
MnV_2O_4	5	4000	73	[22]
$Zn_3V_3O_8$	5	2000	72.6	[23]
$K_{1.15}V_5O_{13}{\cdot}1.3H_2O$.	4	4000	75.8	[24]
$V_2O_5{\cdot}nH_2O$	6	900	71.0	[25]
$Ni_{0.25}V_2O_5{\cdot}0.88H_2O$	10	10000	77.0	[26]
$KV_2O_4PO_4{\cdot}3.2H_2O$ (KVP)	3	3000	75.0	[27]
$Na_6V_{10}O_{28}$	0.1	100	83.8	[28]

Table S8. Estimation of conduction band and valence band positions of MV_2V_{10}-a and MV_2V_{10}-b.

	E^0 red vs. Ag/AgCl (V)	E^0 red vs. NHE (V)	CB (eV) –(E^0 vs. NHE +4.45V)	Band gap (Eg, eV)	VB (eV) –(Eg)+CB
MV_2V_{10}-a	-0.69	-0.49	-3.96	2.07	-6.03
MV_2V_{10}-b	-0.68	-0.48	-3.97	0.68	-4.65

supplementary

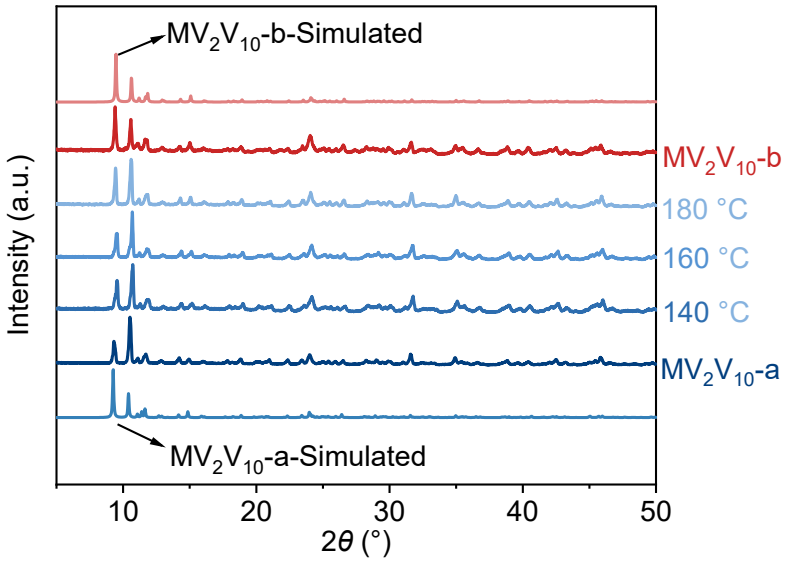

Figure S1. The simulated and experimental PXRD patterns of MV_2V_{10}.

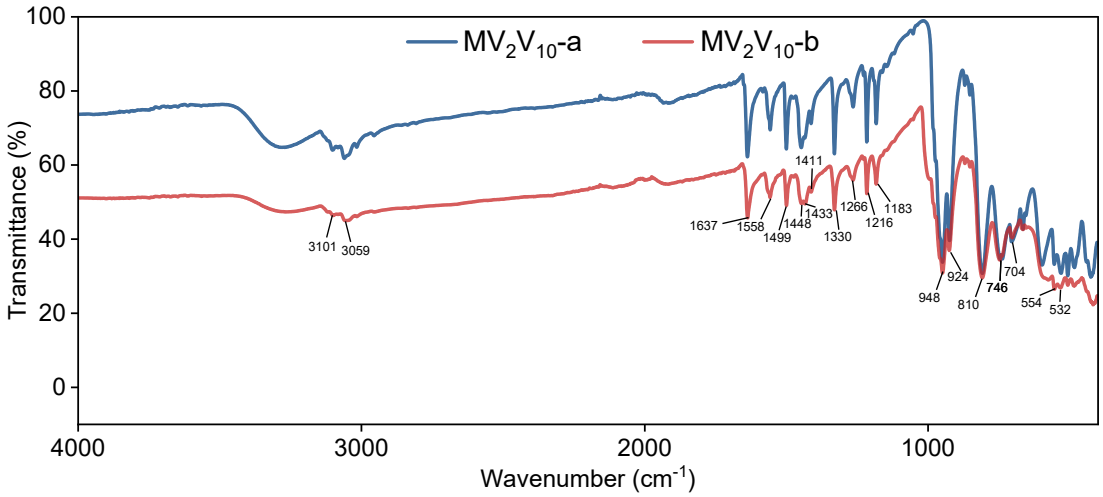

Figure S2. IR spectra of MV_2V_{10}-a and MV_2V_{10}-b.Peaks at 3101, 3059 cm^{-1} ascribe to the *v*(=C-H); peaks at 1637, 1558, 1499 cm^{-1} ascribe to the *v*(pyridine skeleton); peaks at 1448, 1333 cm^{-1} ascribe to the *δ*(C-H) in $–CH_3$; peaks at positions 1350-1100 cm^{-1} mainly ascribe to the *v*(C-N); the peaks below 1000 cm^{-1} mainly ascribe to the *v*(V-O)、*v*(V=O) and partly *δ*(=C-H).

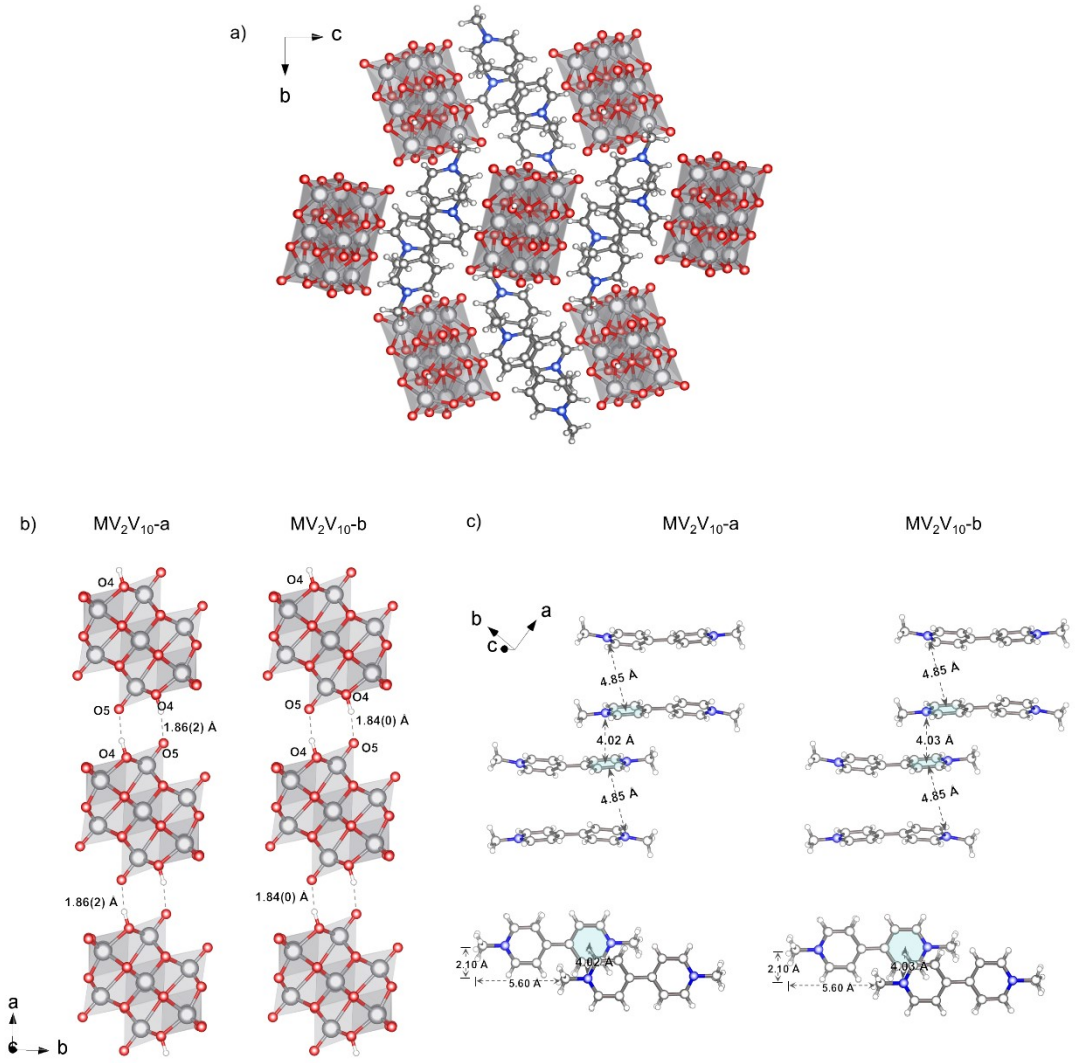

Figure S3. Stacking of the MV_2V_{10} in the *bc*-plane (a), hydrogen-bonded chain networks between $[H_2V_{10}O_{28}]^{4-}$ anions (b), and the interaction between MV^{2+} (c).

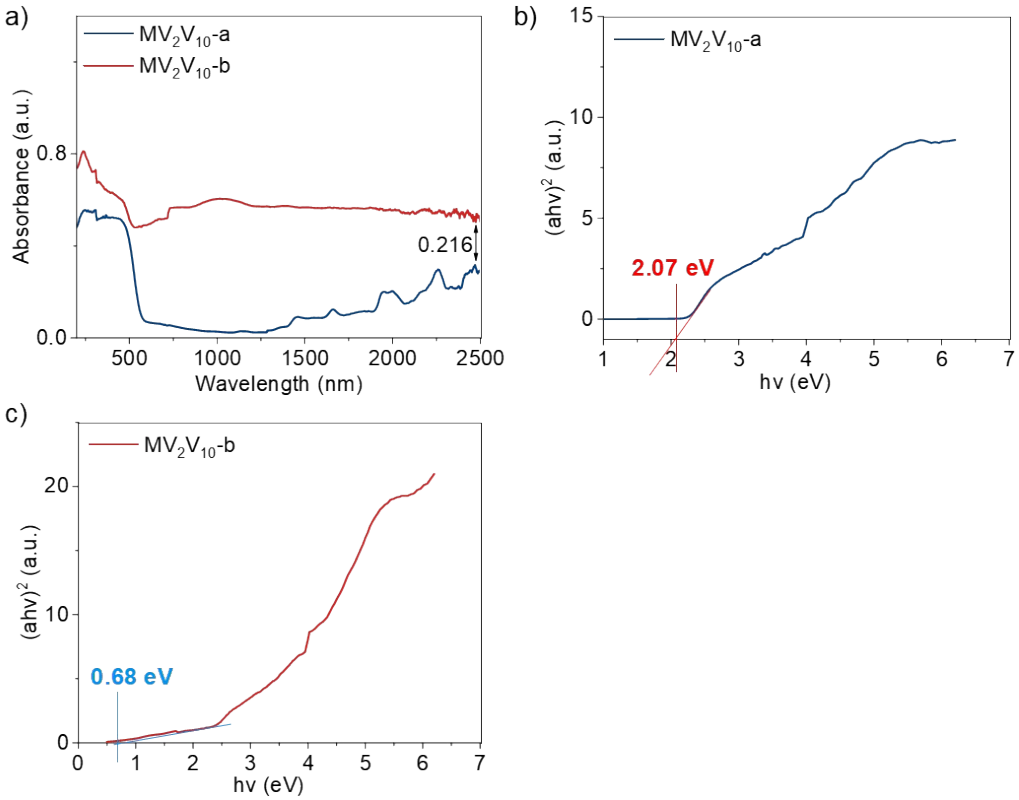

Figure S4. (a) The UV-Vis spectra of MV_2V_{10}-a and MV_2V_{10}-b from 200 to 2500 nanometers. (b) The band gap of MV_2V_{10}-a. (c) The band gap of MV_2V_{10}-b.

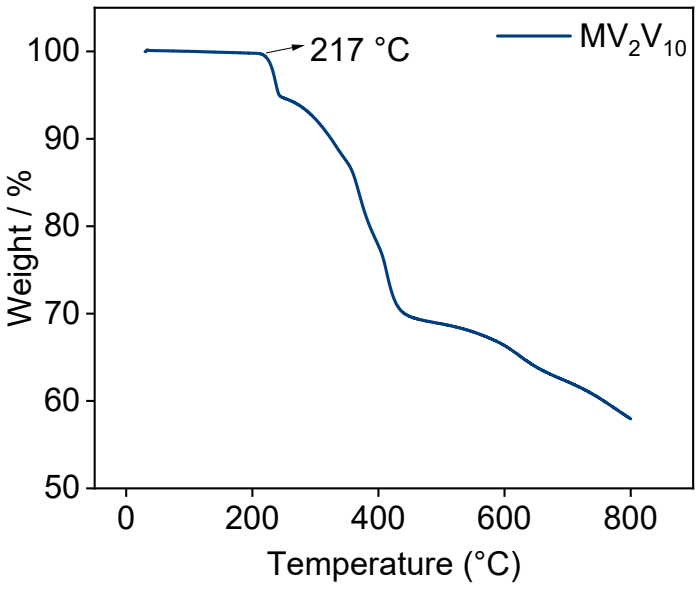

Figure S5. Thermogravimetric analysis of MV_2V_{10}.

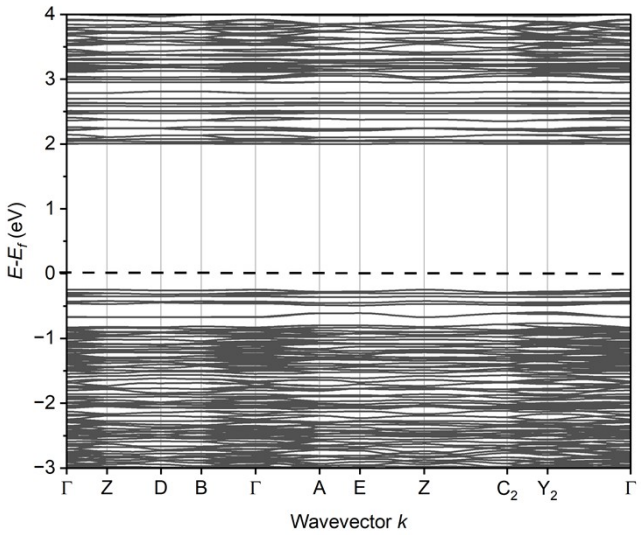

Figure S6. The band structure (BS) of MV_2V_{10}.The Fermi level is set to zero.

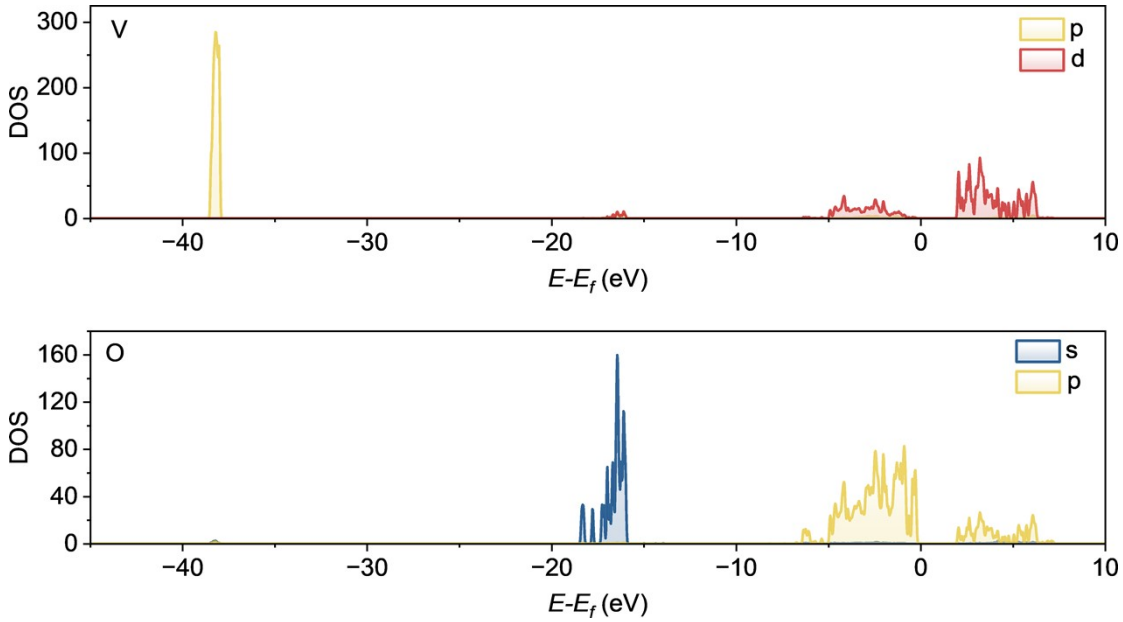

Figure S7. The partial density of states (PDOS) for V atoms, O atoms.The Fermi level is set to zero.

Figure S8. The calculated model of V_{10}, extracted from MV_2V_{10}.

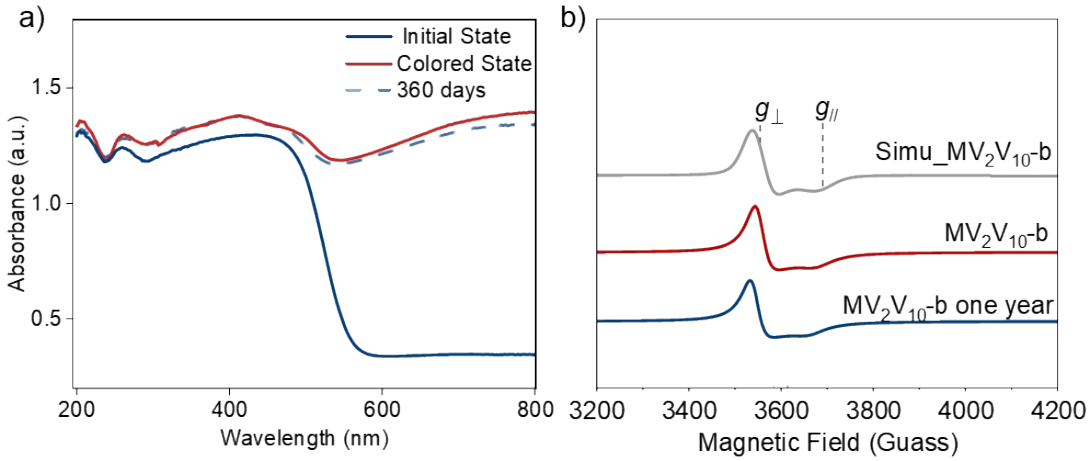

Figure S9. (a) Stability test of charge-separated state. (b) EPR spectra of MV_2V_{10}-b, MV_2V_{10}-b one year and simulated MV_2V_{10}-b, where $[g_\perp, g_{//}]$ = [1.98, 1.91].

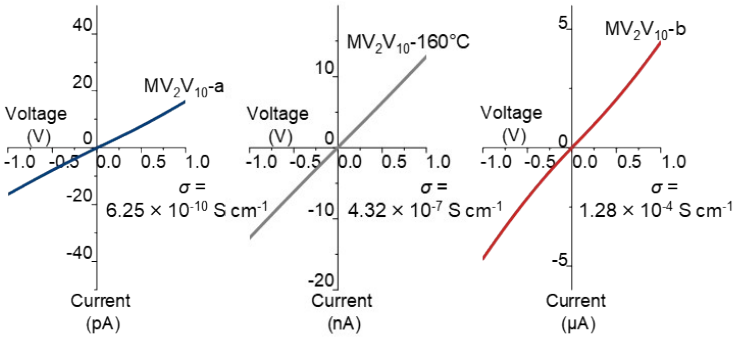

Figure S10. *I-V* curves of pellet sample MV_2V_{10}-a, MV_2V_{10}-b and MV_2V_{10}-160°C. Pellet samples of both MV_2V_{10}-a, MV_2V_{10}-160°C and MV_2V_{10}-b exhibit Ohmic current-voltage (*I-V*) characteristics. Remarkably, the conductivity increased by 691 times (4.32 × 10^{-7} S cm^{-1}) upon annealing at 160°C, the electrical conductivity increases by five orders of magnitude of 205,000-fold from an insulating level (6.25 × 10^{-10} S cm^{-1}) to a semiconducting level (1.28 × 10^{-4} S cm^{-1}) after coloration.

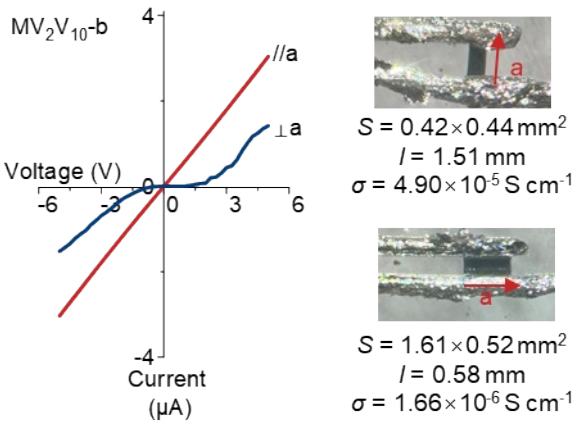

Figure S11. *I-V* curves and photographs of single crystal sample MV_2V_{10}-b, along (∥a) and perpendicular (⊥a) to the *a*-axis.

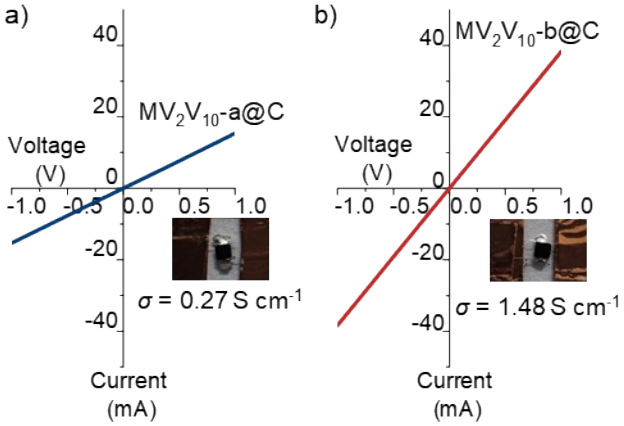

Figure S12. *I-V* curves of pellet sample MV_2V_{10}-a@C and MV_2V_{10}-b@C. To verify the conductivity variation of the composite MV_2V_{10} electrode material, we mixed the components in the same ratio and found that the conductivity of MV_2V_{10}-b@C (1.48 S cm^{-1}) was also significantly improved compared with MV_2V_{10}-a@C (0.27 S cm^{-1}).

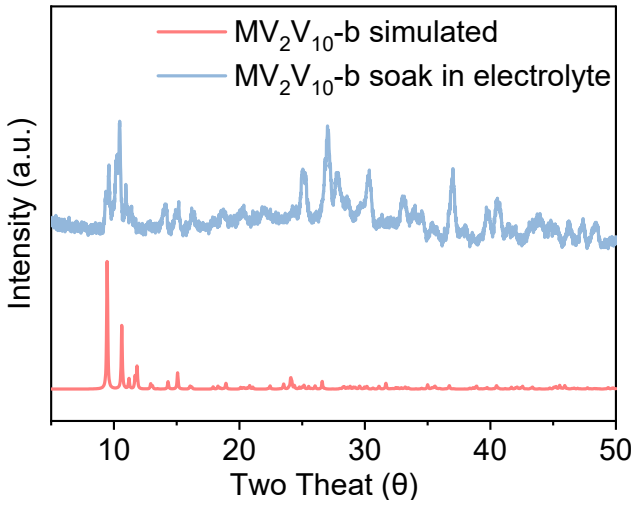

Figure S13. The simulated and experimental PXRD patterns of MV_2V_{10}-b soak in electrolyte.

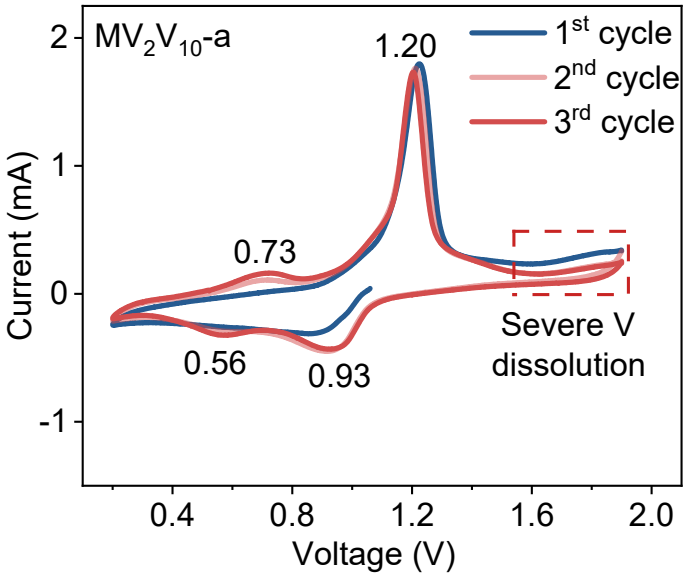

Figure S14. CV curves of MV_2V_{10}-a electrode for first three cycles at a scan rate of 1.0 mV s^{-1} within a voltage range of 0.2–1.9 V.

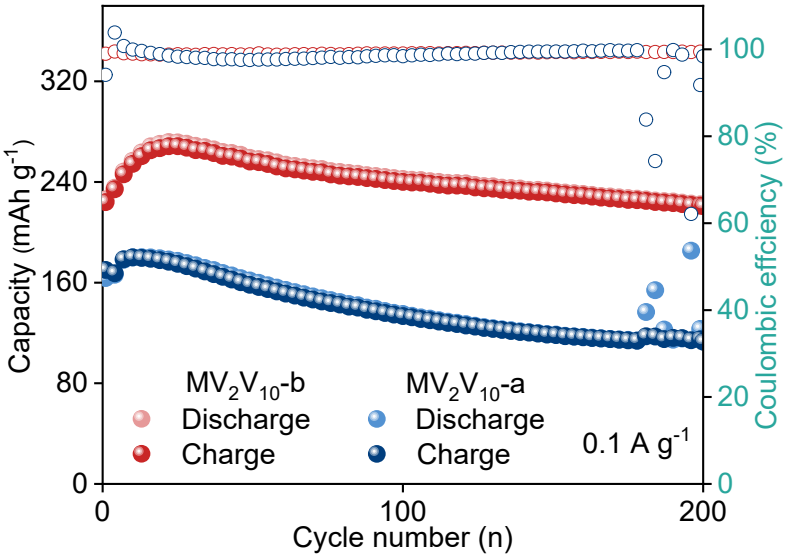

Figure S15. Charge/Discharge curves of the MV_2V_{10}-a and MV_2V_{10}-b cathode with coulombic efficiency at 0.1 A g^{-1}.

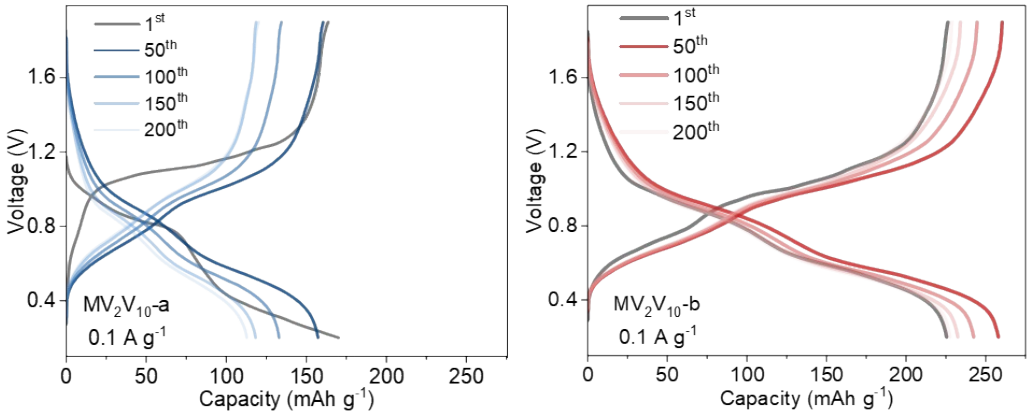

Figure S16. Charge/Discharge curves of the MV_2V_{10}-a and MV_2V_{10}-b cathode at 0.1 A g^{-1}.

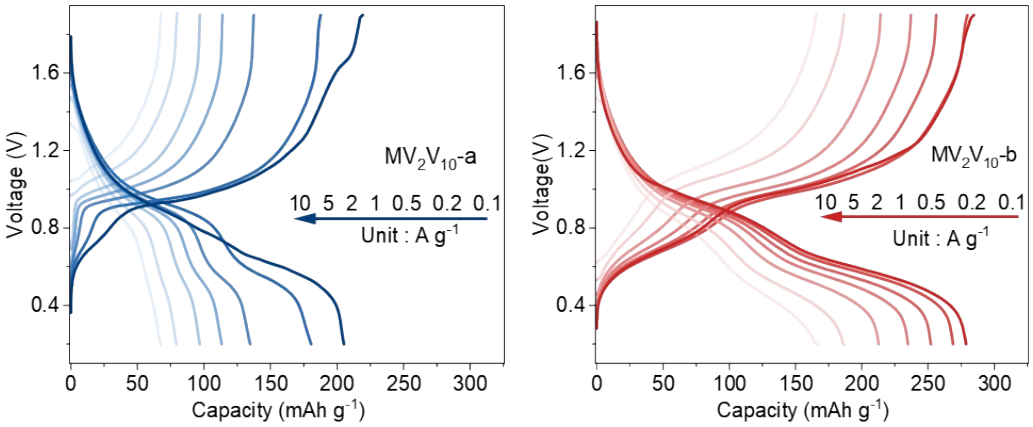

Figure S17. Charge/Discharge curves of the MV_2V_{10}-a and MV_2V_{10}-b cathode at 0.1-10 A g^{-1}.

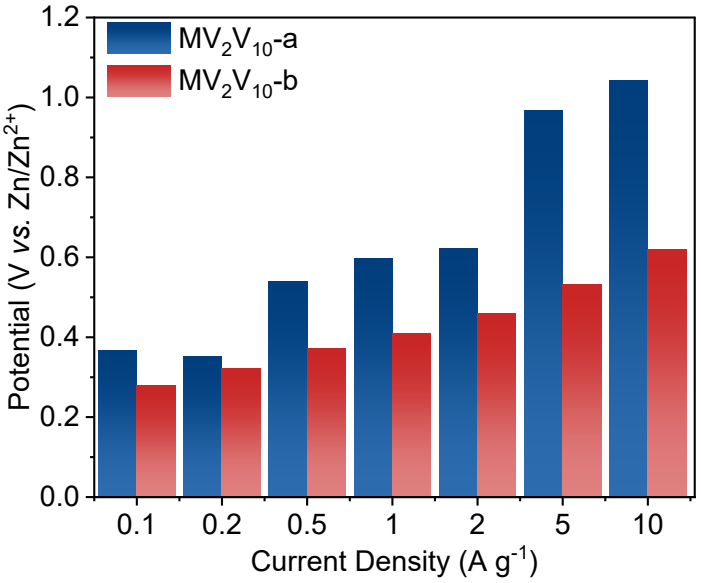

Figure S18. Corresponding polarization voltage for different current densities.

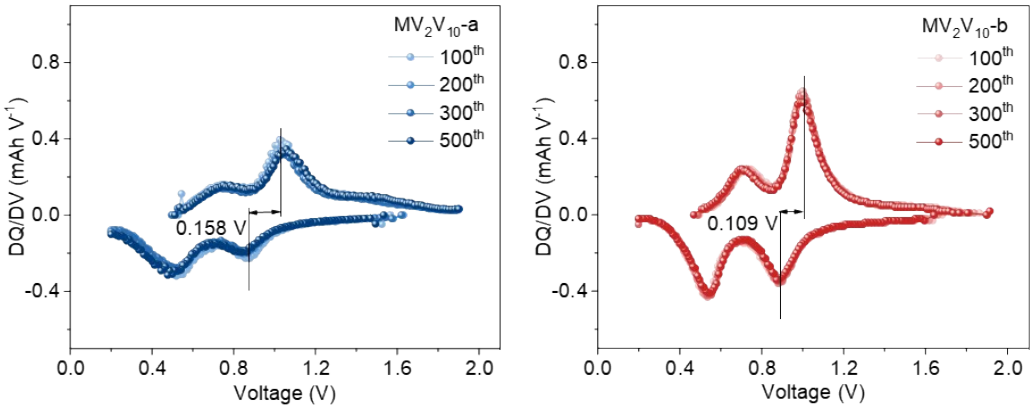

Figure S19. DQ/DV curves of the different cathodes at 2 A g^{-1}.

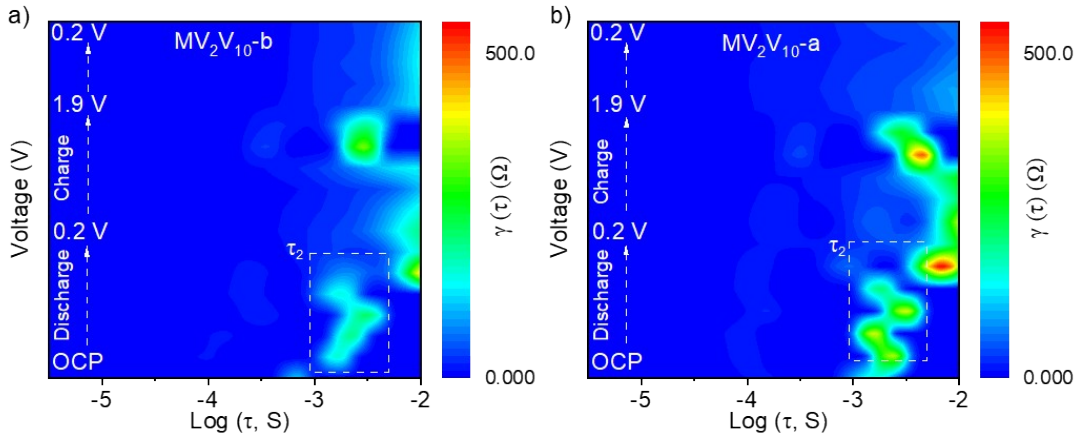

Figure S20. DRT of plots of the EIS of (a) MV_2V_{10}-b and (b) MV_2V_{10}-a at room temperature.

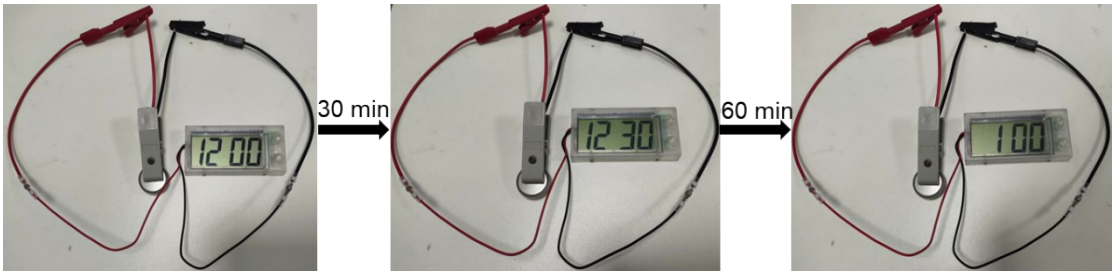

Figure S21. The MV_2V_{10}-b coin cell battery provides continuous power for the digital display for 60 min.

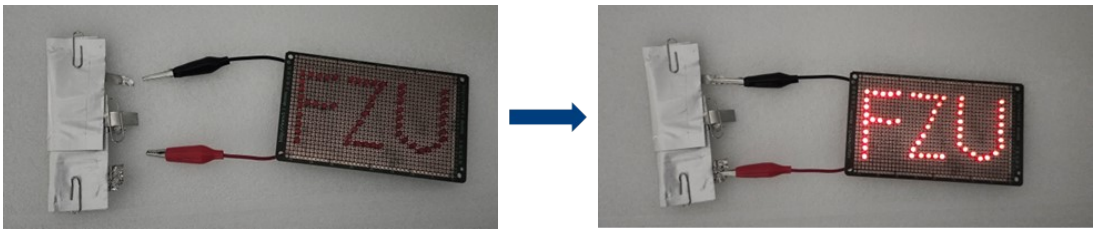

Figure S22. Driving red light bulbs of the soft pack battery (3 × 3 cm^{-2}) in bent 180° state.

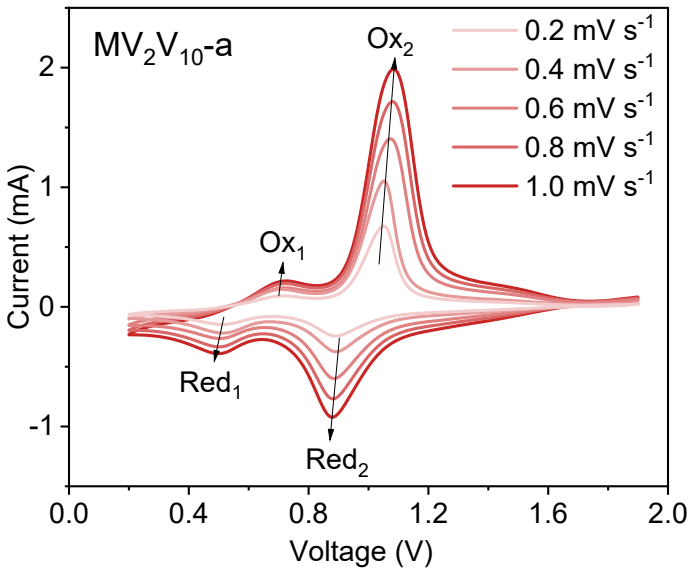

Figure S23. CV curves of MV_2V_{10}-a at different scan rates from 0.2 to 1.0 mV s^{-1}.

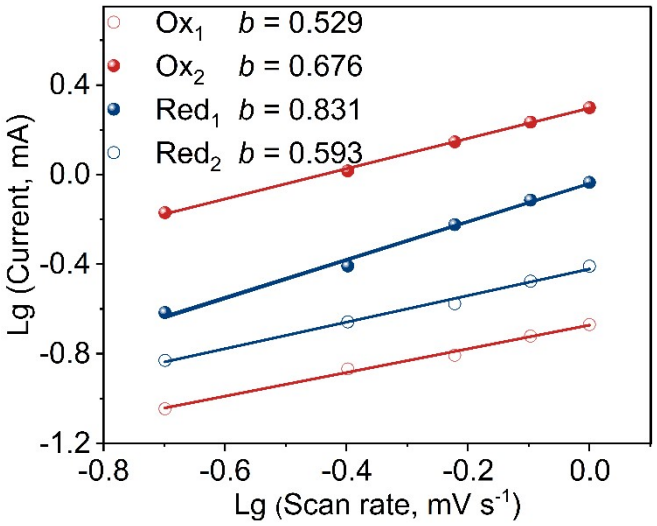

Figure S24. Plots of log(*i*) vs log(*v*) of the current response at the four peaks shown in Figure S19.

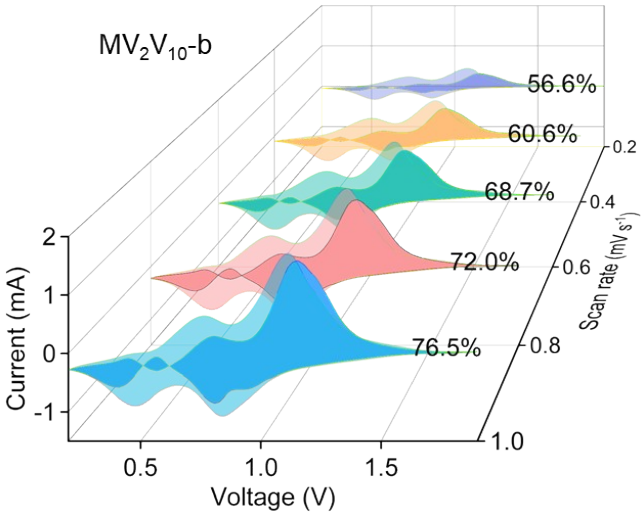

Figure S25. Capacitive contribution at different scan rates for MV_2V_{10}-b.

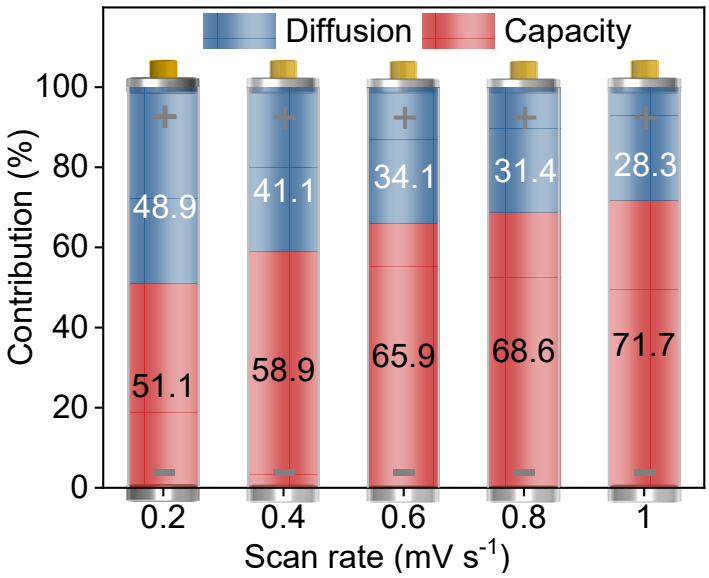

Figure S26. Capacity contribution ratios at different scan rates for MV_2V_{10}-a.

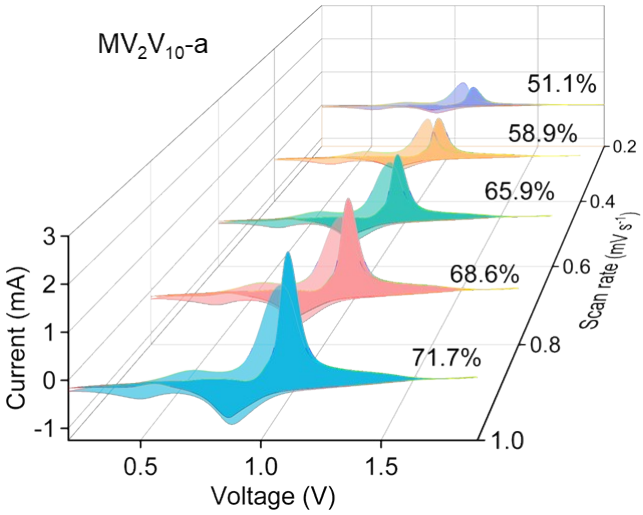

Figure S27. Capacitive contribution at different scan rates for MV_2V_{10}-a.

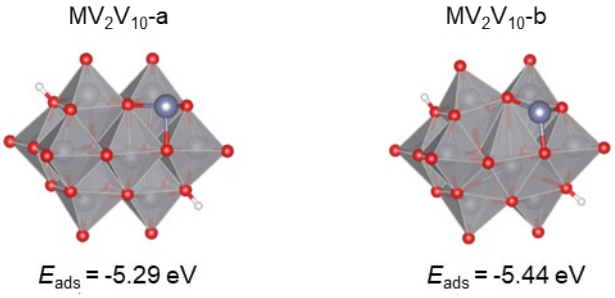

Figure S28. Calculated adsorption energy of Zn^{2+}.

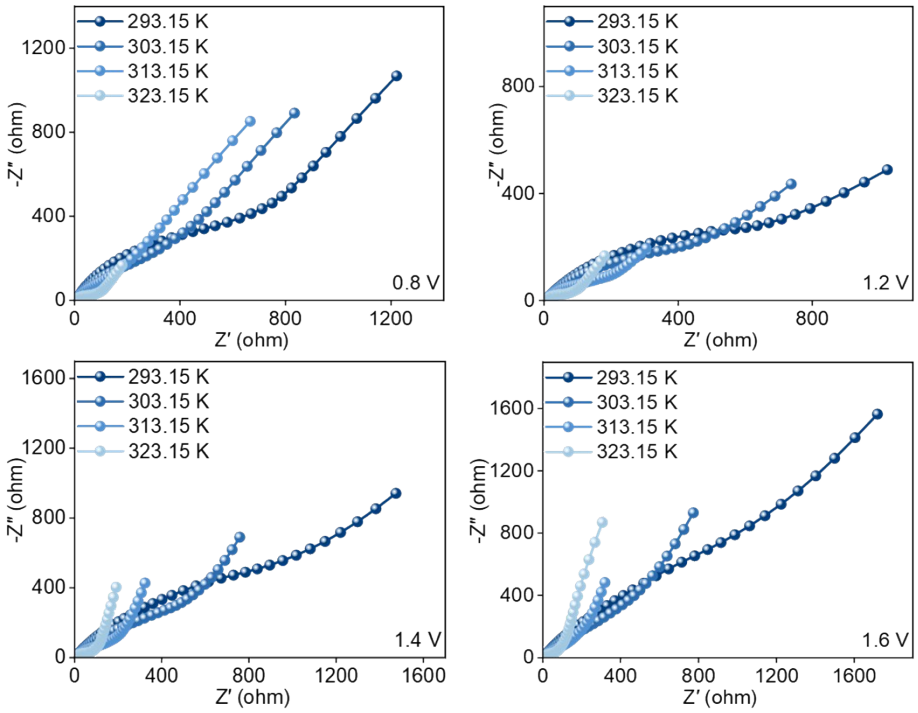

Figure S29. EIS plots of MV_2V_{10}-a at different temperature gradients of 0.8 V, 1.2 V, 1.4 V, and 1.6 V, respectively.

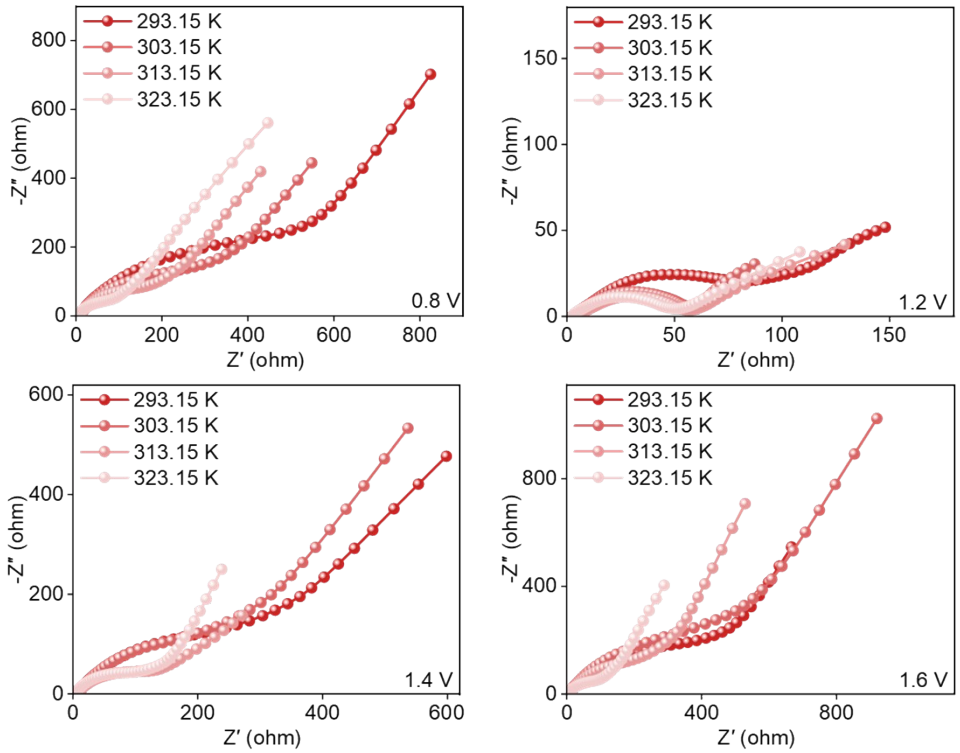

Figure S30. EIS plots of MV_2V_{10}-b at different temperature gradients of 0.8 V, 1.2 V, 1.4 V, and 1.6 V, respectively.

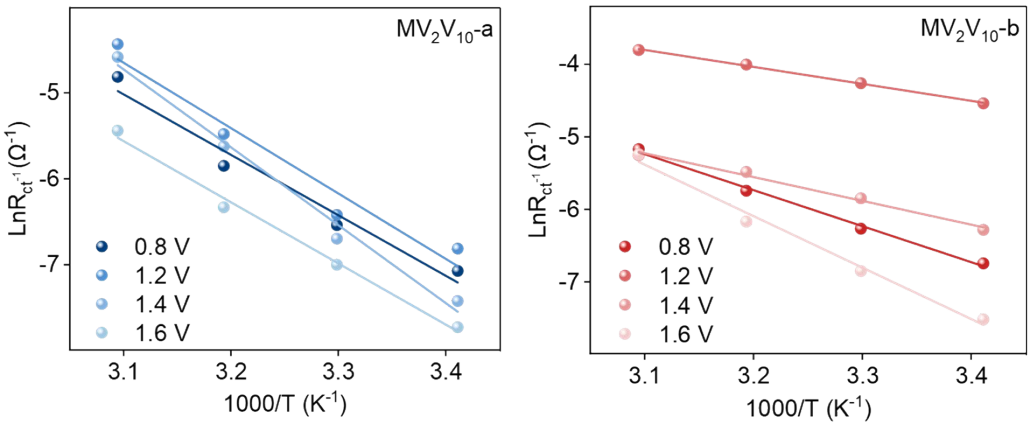

Figure S31. Arrhenius curves at different voltage for MV_2V_{10}-a and MV_2V_{10}-b cathode.

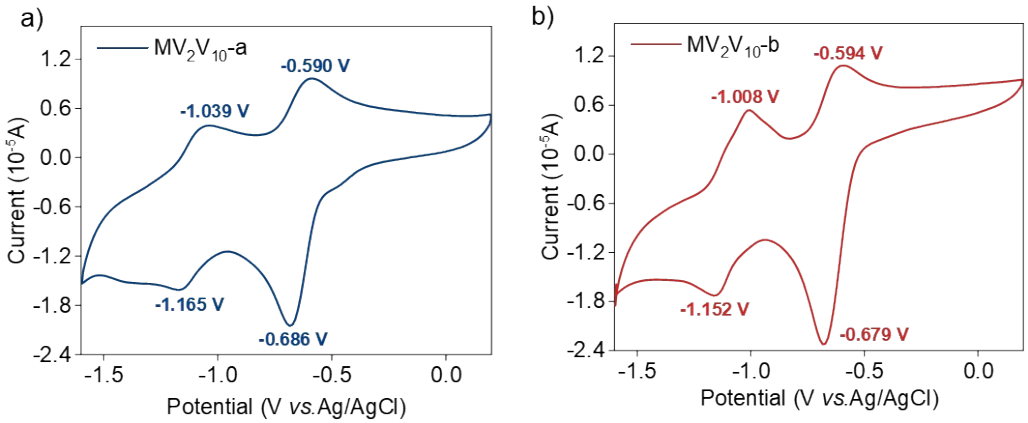

Figure S32. (a-b) CV curve of MV_2V_{10}-a and MV_2V_{10}-b used as working electrodes at 20 mV s^{-1} in 0.2 M $KHCO_3$ aqueous solution.

References

1. T. Hagemann, J. Winsberg, M. Grube, I. Nischang, T. Janoschka, N. Martin, M. D. Hager and U. S. Schubert, *J. Power Sources*, 2018, **378**, 546-554.
2. K. Zhang, M. Park, L. Zhou, G. H. Lee, W. Li, Y. M. Kang and J. Chen, *Adv. Funct. Mater.* , 2016, **26**, 6728-6735.
3. Y. Ding, C. Cai, L. Ma, J. Wang, M. P. Mercer, J. Liu, D. Kramer, X. Yu, D. Xue, C. Zhi and C. Peng, *Adv.Energy Mater.* , 2025, **15**, 2402819.
4. W. Wang, P. Li, H. Zheng, Q. Liu, F. Lv, J. Wu, H. Wang and S. Guo, *Small*, 2017, **13**, 1702228.
5. J. P. Perdew, K. Burke, Y. Wang, *Phys. Rev. B* **1996**, *54*, 16533-16539.
6. Klimes, J.Bowler, D. R.Michaelides, *A.J. Phys.: Condens. Matter* **2010**, *22*, 022201.
7. M. J. Frisch, G. W. Trucks, H. B. Schlegel, G. E. Scuseria, M. A. Robb, J. R. Cheeseman, G. Scalmani, V. Barone, G. A.Petersson, H. Nakatsuji, X. Li, M. Caricato, A. Marenich, J. Bloino, B. G. Janesko, R. Gomperts, B. Mennucci, H. P. Hratchian, J. V. Ortiz, A. F. Izmaylov, J. L. Sonnenberg, D. Williams-Young, F. Ding, F. Lipparini, F. Egidi, J. Goings, B.Peng, A. Petrone, T. Henderson, D. Ranasinghe, V. G. Zakrzewski, J. Gao, N. Rega, G. Zheng, W. Liang, M. Hada, M.Ehara, K. Toyota, R. Fukuda, J. Hasegawa, M. Ishida, T. Nakajima, Y. Honda, O. Kitao, H. Nakai, T. Vreven, K. Throssell, J. A. Montgomery, Jr. Peralta, J. E, F. Ogliaro, M. Bearpark, J. J. Heyd, E. Brothers, K. N. Kudin, V. N. Staroverov, T. Keith, R. Kobayashi, J. Normand, K. Raghavachari, A. Rendell, J. C. Burant, S. S. Iyengar, J. Tomasi, M. Cossi, J. M. Millam, M. Klene, C. Adamo, R. Cammi, J. W. Ochterski, R. L. Martin, K. Morokuma, O. Farkas, J. B. Foresman, D. J. Fox, Gaussian 09, Revision D.01; Gaussian, Inc.: Wallingford, CT, 2009.
8. T. Lu and F. Chen, *J. Comput. Chem.*, 2011, **33**, 580-592.
9. C. Sun, X. Q. Yu, M. S. Wang and G. C. Guo, *Angew. Chem. Int. Ed.*, 2019, **58**, 9475-9478.
10. C. Sun, G. Xu, X.-M. Jiang, G.-E. Wang, P.-Y. Guo, M.-S. Wang and G.-C. Guo, *J. Am. Chem. Soc.*, 2018, **140**, 2805-2811.
11. C. Jia, A. Migliore, N. Xin, S. Huang, J. Wang, Q. Yang, S. Wang, H. Chen, D. Wang, B. Feng, Z. Liu, G. Zhang, D.-H. Qu, H. Tian, M. A. Ratner, H. Q. Xu, A. Nitzan and X. Guo, *Science*, 2016, **352**, 1443−1445.
12. I. Chung, J.-H. Song, J. Im, J. Androulakis, C. D. Malliakas, H. Li, A. J. Freeman, J. T. Kenney and M. G. Kanatzidis, *J. Am. Chem. Soc.*, 2012, **134**, 8579-8587.
13. H. Jiang, C. Sun, C.-M. Yu, M.-S. Wang and G.-C. Guo, *Inorg. Chem.*, 2021, **60**, 5538-5544.
14. C. Sun, M. S. Wang, P. X. Li and G. C. Guo, *Angew. Chem. Int. Ed.*, 2017, **56**, 554-558.
15. Y. F. Sang, H. Zeng, L. J. Xu and Z. N. Chen, *Adv. Funct. Mater.* , 2022, **32**, 2206459.
16. Q. P. Qin, J. Lu, C. Sun, M. S. Wang and G. C. Guo, *Small*, 2023, **20**, 2307333.
17. Q. Zhang, S. Ju, S. Zhang, S. Xu and Z. Zhang, *Adv.Energy Mater.* , 2025, **15**, 2404597.
18. D. Kundu, B. D. Adams, V. Duffort, S. H. Vajargah and L. F. Nazar, *Nat. Energy*, 2016, **1**, 16119
19. N. Zhang, F. Cheng, Y. Liu, Q. Zhao, K. Lei, C. Chen, X. Liu and J. Chen, *J. Am. Chem. Soc.*, 2016, **138**, 12894-12901.
20. Y. Zhang, Q. Li, W. Feng, H. Yue, S. Gao, Y. Su, Y. Tang, J. Wu, Z. Zhang, Y. Zhang, M. Shakouri, H. C. Chen and H. Pang, *Angew. Chem. Int. Ed.*, 2025, **64**, e202501728.
21. C. Li, X. Yun, Y. Chen, D. Lu, Z. Ma, S. Bai, G. Zhou, P. Xiao and C. Zheng, *Chem. Eng. J.*, 2023, **477**, 146901.
22. S. Wei, S. Chen, X. Su, Z. Qi, C. Wang, B. Ganguli, P. Zhang, K. Zhu, Y. Cao, Q. He, D. Cao, X. Guo, W. Wen, X. Wu, P. M. Ajayan and L. Song, *Energy Environ. Sci.*, 2021, **14**, 3954-3964.
23. J. Wu, Q. Kuang, K. Zhang, J. Feng, C. Huang, J. Li, Q. Fan, Y. Dong and Y. Zhao, *Energy Storage Mater.*, 2021, **41**, 297-309.
24. N. Qiu, Z. Yang, R. Xue, Y. Wang, Y. Zhu and W. Liu, *Nano Lett.*, 2021, **21**, 2738-2744.
25. M. Yan, P. He, Y. Chen, S. Wang, Q. Wei, K. Zhao, X. Xu, Q. An, Y. Shuang, Y. Shao, K. T. Mueller, L. Mai, J. Liu and J. Yang, *Adv. Mater.*, 2017, **30**, 1703725.
26. J. Feng, Y. Wang, S. Liu, S. Chen, N. Wen, X. Zeng, Y. Dong, C. Huang, Q. Kuang and Y. Zhao, *ACS Appl. Mater. Interfaces*, 2020, **12**, 24726-24736.
27. X. Yang, W. Deng, M. Chen, Y. Wang and C. F. Sun, *Adv. Mater.*, 2020, **32**, 2003592.
28. T. Zhou, L. Xie, Q. Han, X. Yang, L. Zhu and X. Cao, *Chem. Eng. J.*, 2022, **445**, 136789.